THE JOURNAL OF
PHYSICAL
CHEMISTRY A

VOLUME 107, NUMBER 28, JULY 17, 2003

ARTICLES

Dynamics Study of the Reaction $S + O_2 \rightarrow SO + O$ and Its Reverse on a Single-Valued Double Many-Body Expansion Potential Energy Surface for Ground-State SO_2

S. P. J. Rodrigues and A. J. C. Varandas*

Departamento de Química, Universidade de Coimbra, 3004-545 Coimbra, Portugal

Received: January 31, 2003; In Final Form: April 21, 2003

Quasiclassical trajectory calculations have been carried out for the reaction $S + O_2 \rightarrow SO + O$ and its reverse using an accurate single-valued double many-body expansion (DMBE) potential energy surface previously reported for the ground electronic state of the sulfur dioxide molecule. A new scheme is suggested for thermalization of the reactants which avoids the usual separation of rotation and vibration. A detailed analysis of complex formation and thermal energy distribution in the products is also presented for the direct reaction at $T = 300$ *K*. The agreement with experimental data is satisfactory.

1. Introduction

The elementary reactions involving the sulfur dioxide (SO_2) molecule have an important role in the combustion of sulfur-containing materials.[1] In particular, the title reaction has been the subject of much experimental work,[2−10] from which critical evaluations of the results have also been reported.[11,12] Theoretically, it has been studied by Murrell and co-workers[13,14] using the quasiclassical trajectory method and two different many-body expansion (MBE) potential energy surfaces[13,15] which were calibrated from fits to spectroscopic data and limited ab initio energies. Similar studies were reported by Lendvay et al.[16] using a MBE potential energy surface calibrated from extensive ab initio calculations. Although other potential energy surfaces have been reported based on spectroscopic data[17−19] and ab initio energies,[20] they are valid only over limited regions of configurational space and hence cannot be used per se for reaction dynamics studies.

Recently,[21,22] we have reported a single-valued double many-body expansion[23−25] (DMBE) potential energy surface for ground state SO_2 calculated from a multiproperty fit to extensive ab initio correlated energies and spectroscopic data. This surface is believed[21,22] to describe accurately most topographical features of the system including the dissociation channels and will be used here to study the dynamics of the title reaction and its reverse. For this, we employ the quasiclassical trajectory method as the atoms are sufficiently heavy to validate such an approach. The emphasis will be on thermalized calculations, for which a new scheme that avoids the usual separation of rotation and vibration is suggested to perform the thermalization of the reactants. We also investigate the problem of complex formation, and carry out a detailed analysis of the products energy distribution for the direct reaction at $T = 300$ K.

The paper is organized as follows. In section 2, we summarize some relevant details of the DMBE potential energy surface. The quasiclassical trajectory methodology is described in section 3. Section 4 summarizes the calculations, while the conclusions are in section 5.

2. Potential Energy Surface

The main features of the DMBE potential energy surface for SO_2 have been discussed in detail elsewhere,[21] and hence, we concentrate here on the features that are relevant for the dynamics studies of the title reactions. A graphical view of the

---

* E-mail: varandas@qtvs1.qui.uc.pt.

10.1021/jp0301305 CCC: $25.00

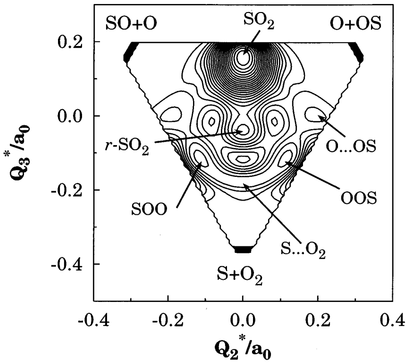

Figure 1. Relaxed contour plot[26] of the SO$_2$ potential energy surface in reduced linear symmetry coordinates: $Q_2^* = (R_2 - R_1)/\sqrt{2}P$, $Q_3^* = (2R_3 - R_2 - R_1)/\sqrt{6}P$, and $P = R_1 + R_2 + R_3$.

potential is shown in Figure 1 as a relaxed triangular plot[26] employing the reduced linear symmetry coordinates $Q_2^* = (R_2 - R_1)/\sqrt{2}P$ and $Q_3^* = (2R_3 - R_2 - R_1)/\sqrt{6}P$, where $P = R_1 + R_2 + R_3$ is the molecular perimeter. Clearly visible in this plot are the dissociation channels (in the vicinity of the vertexes of the triangle that circumscribes the physical space), and the various minima of the potential energy surface which are indicated by arrows. From this figure, and the minimum energy paths shown in Figure 6 of ref 21, it is possible to verify that the DMBE potential energy surface shows no barrier both for the S + O$_2$ and O + SO reactions, a result that is in agreement with the surfaces of Lendvay, Schatz, and Harding (LSH)[16] and Murrell, Craven, and Zhu (MCZ).[15] Note that all these potential energy surfaces disagree with an early function reported by Murrell et al.[13] which shows a nonphysical barrier along the S + O$_2$ reaction channel. Thus, we will not make any further reference to this function even during the discussion of the results. In fact, the experimental measurements and their dependence on temperature[7] lead one to expect that the title reactions should occur without any significant barrier for some angles, although the S + O$_2$ reaction has probably a narrow entrance channel. Note also that the significant barrier encountered for the collinear S + O$_2$ approach in the DMBE potential energy surface is in agreement with the LSH surface but not with the MCZ one. This may probably be explained by the fact that the long-range regions of the MCZ surface have been modeled from the requirement that there should be no barrier for some angles of approach, and not from a fit to ab initio energies (these clearly support the existence of a barrier at such regions[16,21,22]). Also in agreement with the LSH surface, but again at divergence with the MCZ surface, is the existence of a significant barrier for the collinear O + OS approach. All potential energy surfaces predict the collinear O + SO approach to be barrierless. We note that the major qualitative difference between the DMBE and LSH potential energy surfaces lies perhaps on the fact that the latter shows a high barrier for C_{2v} insertion of S into O$_2$, a feature that is shared by the MCZ surface. This is not the case in DMBE, although it shows a significant barrier for short atom−diatom C_{2v} geometries due to a crossing which originates the ring r − SO$_2$ isomer. A final remark to note is that the "chemical regions" of the DMBE, LSH, and MCZ potential energy surfaces are all qualitatively similar, namely in what refers to the minima associated with the various isomeric species. However, the DMBE potential energy surface is expected to provide there the most reliable description, as it shows near-spectroscopic accuracy at the global minimum. We emphasize that the DMBE potential energy surface has been modeled from a fit to ab initio energies under the constraint that the calculated vibrational levels should accurately reproduce those observed in the spectra of the most stable SO$_2$ isomer. It should also be pointed out at this stage that we have introduced a tiny modification into the DMBE potential energy surface[21] in order to avoid numerical problems in the calculation of the electrostatic energy term, which is not well-defined at linear geometries. To do this a scaling of the Jacobi angle was introduced, namely $\cos\theta' = [0.99 + 0.01(1 - \cos^6\theta)]\cos\theta$; this eliminates the problem without perturbing the potential at other regions of configurational space.

3. The Quasiclassical Trajectory Method

The quasiclassical trajectory (QCT) method is a standard and well documented tool[27−29] for carrying out studies of reaction dynamics. For the QCT calculations carried out in the present work, we have used an extensively modified version (see refs 30 and 31 for previous modifications) of the MERCURY code.[32] In particular, improvements have been introduced on the thermalization of reactants, and the monitoring of complex formation (see section 3.1).

The thermal rate coefficient for the reaction S + O$_2$ → O + SO can be calculated from the expression

$$k(T) = g(T)\left(\frac{8k_BT}{\pi\mu_{S-O_2}}\right)^{1/2}\sum_{vj}(2j+1)\times \frac{e^{-E_{vj}/k_BT}}{Q_{vr}}\int dE_{tr}\frac{E_{tr}}{(k_BT)^2}e^{-E_{tr}/k_BT}\sigma(E_{tr}, v, j) \quad (1)$$

where

$$g(T) = 1/\{3[5 + 3\exp(-570/T) + \exp(-825/T)]\} \quad (2)$$

is the appropriate electronic degeneracy factor which has been obtained according to the usual procedure;[33,34] the atomic levels of sulfur have been taken from refs 35 and 36. Note that other authors[13,15,16] employed the high-temperature limit factor $g = 1/27$. In turn, $Q_{vr} = \sum_{vj}(2j + 1)\exp(-E_{vj}/k_BT)$ is the vibrational−rotational partition function of O$_2$, and $\sigma(E_{tr}, v, j)$ is the reactive cross-section. As usual, E_{tr} denotes the relative translational energy, μ_{S-O_2} the atom−diatom reduced mass, and E_{vj} the vibrational−rotational energy of O$_2$ with v and j specifying the vibrational and rotational quantum numbers. Note further that j takes only odd values for O$_2$ due to its nuclear statistics.

The thermal rate coefficient for the reaction O + SO → S + O$_2$ has been calculated in a similar manner but using the vibrational−rotational partition function of SO, and the appropriate degeneracy factor $g(T)$ which is similar to the one for the O + O$_2$ reaction.[37]

3.1. Thermalized Calculations. We have sampled E_{tr} from the Maxwell−Boltzmann distribution using[29]

$$E_{tr} = -k_BT\ln(\xi_1\xi_2) \quad (3)$$

where ξ_1 and ξ_2 are freshly generated random numbers; for an alternative approach to generate such a distribution, see ref 38. The vibrational−rotational energy E_{vr} distribution has been sampled from the corresponding Boltzmann distribution. To avoid the traditional approximation concerning the separation of rotational and vibrational energies, the vibrational−rotational energy levels E_{vj} of the diatomics have been calculated and ordered by their energy values prior to running the trajectory

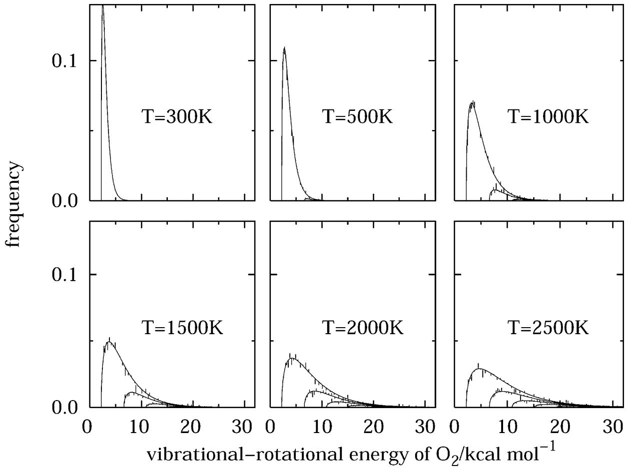

Figure 2. Generated and exact (within the model) vibrational–rotational energy distributions. The latter are represented for each vibrational quantum number v as the line envelope of the rotational quantum numbers j, while the former is indicated by the vertical displacements from that curve (see text).

batches. The levels have then been sampled using the cumulative distribution function[27,29]

$$\sum_{v_0,j_0}^{v,j}(2j+1)\frac{e^{-E_{vj}/k_\mathrm{B}T}}{Q_\mathrm{vr}}=\xi_3 \tag{4}$$

where the summation runs from the lowest energy level characterized by the quantum numbers (v_0, j_0) to the level (v, j) which gives the best agreement with the random number $0 \le \xi_3 \le 1$. For the present study, E_{vj} has been calculated from the expression for a vibrating–rotating (vib–rotor) Morse potential, namely

$$E_{vj}=\omega_\mathrm{e}\left(v+\frac{1}{2}\right)-\omega_\mathrm{e}x_\mathrm{e}\left(v+\frac{1}{2}\right)^2+B_\mathrm{e}\,j(j+1)-\alpha_\mathrm{e}\left(v+\frac{1}{2}\right)j(j+1)-D_\mathrm{e}[j(j+1)]^2 \tag{5}$$

where $\omega_\mathrm{e} = 1563.33$ cm^{-1}, $\omega_\mathrm{e}x_\mathrm{e} = 14.57$ cm^{-1}, $B_\mathrm{e} = 1.44574$ cm^{-1}, $\alpha_\mathrm{e} = 0.01742$ cm^{-1}, and $D_\mathrm{e} = 4.93 \times 10^{-6}$ cm^{-1} are, in the usual notation,[39] the spectroscopic constants of the EHFACE2U diatomic curve for O_2; for the EHFACE2U SO diatomic curve, these constants assume the values $\omega_\mathrm{e} = 1141.45$ cm^{-1}, $\omega_\mathrm{e}x_\mathrm{e} = 7.45$ cm^{-1}, $B_\mathrm{e} = 0.72084$ cm^{-1}, $\alpha_\mathrm{e} = 0.00605$ cm^{-1}, and $D_\mathrm{e} = 1.15 \times 10^{-6}$ cm^{-1}. Note that, within this approach, exact quantum calculated energies can also be utilized with not much extra computational effort, as well as other probability distributions (e.g., non-Boltzmann ones). Besides the fact that the Morse vib–rotor model leads to small errors, one may also benefit from the possibility of using the semiclassical diatomic internuclear distance sampling method of Porter et al.[40] as implemented in the MERCURY[32] code.

A comparison of the generated and exact (taken as the Morse vib–rotor model) distributions of vibrational–rotational energies for O_2 at several temperatures is shown in Figure 2. Of course, such distributions are discrete but due to their compactness the exact one is represented for clarity for each value of v as the line-envelope of the j-distribution while the generated one is represented by the vertical displacements from that line-envelope curve. As can be seen, the generated distributions are very accurate, even for high temperatures where several vibrational quantum numbers are sampled, and the usual separation of vibration and rotation is known to fail.

TABLE 1: Reaction Channels with Energies Referred to the SO_2 Minimum (the Labels *a* and *b* Distinguish the Oxygen Atoms)

channel no.	products	ΔE/kcal mol^{-1}
1	$S + O_2$	139.07
2	$O_a + SO_b$	134.41
3	$O_b + SO_a$	134.41
4	$S + O_a + O_b$	259.29

TABLE 2: Definition of the Reactive Channels (the First Entry Specifies Their Configurational Properties While the Second Entry Defines the Actual Geometries Used)

channel no.	products	R_{SO_a}/Å	R_{SO_b}/Å	R_{OO}/Å
1	$S + O_2$	∞	∞	1.2075
		>10.0	>10.0	<3.0875
2	$O_a + SO_b$	∞	1.4811	∞
		>11.55	<1.7888	>11.55
3	$O_b + SO_a$	1.4811	∞	∞
		<1.7888	>11.55	>11.55
4	$S + O_a + O_b$	∞	∞	∞
		>10.00	>10.00	>10.00

Finally, within the thermalized classical trajectory approach, the thermal rate coefficient is calculated as

$$k(T)=g\left(\frac{8k_\mathrm{B}T}{\pi\mu_{\mathrm{S-O_2}}}\right)^{1/2}\frac{N_\mathrm{r}}{N_\mathrm{t}}\pi {b_\mathrm{max}}^2 \tag{6}$$

where N_r denotes the number of reactive trajectories, N_t the total number of trajectories, and b_max the maximum impact parameter (this has been optimized by running small batches of trajectories for fixed b_max values until the reactivity becomes negligibly small). As usual, the estimate of the error of the thermal rate constant is given by $\Delta k(T) = k(T)[(N_\mathrm{t} - N_\mathrm{r})/N_\mathrm{t}N_\mathrm{r}]^{1/2}$.

3.2. Assignment of Reactive Channels and Monitoring of Complex Formation. The procedure employed to assign the reactive channels is identical to that reported in previous work[30,31,41] for other reactive systems. The SO_2 molecule has four reactive channels (including the atomization one) and their assignment is done here in terms of energetics (see Table 1), and configurational properties (see Table 2). Similarly, the monotoring of complex formation uses both geometrical and energetic criteria to distinguish the various SO_2 isomers. Specifically, the geometric criteria employs reduced symmetry coordinates,[26] with the conditions for formation of a complex being

$$[(Q_2^*-Q_{2,i}^*)^2+(Q_3^*-Q_{3,i}^*)^2]^{1/2}\le S_i \tag{7}$$

$$V(\mathbf{R})\le E_i \tag{8}$$

where $Q_{2,i}^*$ and $Q_{3,i}^*$ are constants that define the equilibrium geometry of the ith complex, S_i is the radius of the circle associated with its configurational space (also in reduced coordinates), and E_i is the maximum allowed energy. Clearly, the geometrical parameters ($Q_{2,i}^*$ and $Q_{3,i}^*$) are obtained from the configurational properties of the associated minima in the potential energy surface. The radius S_i and energy E_i have been selected for each complex by warranting that they are uniquely defined as much as possible. This has been done by an eye-inspection of exploratory trajectories, which has shown that all reported complexes could be well identified through the above requirements. The numerical parameters obtained in this way are presented in Table 3.

4. Results

The numerical results for the thermalized rate constants of the reaction $S + O_2 \rightarrow SO + O$ are presented in Table 4. The

TABLE 3: Parameters Used to Define the Complex Region for the Relevant Minima of the Potential Energy Surface (Energies Are Referred to the SO_2 Minimum)

minima	$Q^*_{2,i}$	$Q^*_{3,i}$	S_i	E_i/kcal mol^{-1}
SO_2	0.0000	0.1542	0.12	125.5
r-SO_2	0.0000	−0.0370	0.04	131.8
SOO	−0.1156	−0.1159	0.08	138.1
OOS	0.1156	−0.1159	0.08	138.1

TABLE 4: Trajectory Results for the $S + O_2$ Reaction[a]

T/K	$g(T)$	b_{max}/Å	N_t	$N_{r,s}$	$k_s(T)/10^{-12}$ cm^3 s^{-1}
50	15.00	8.6	6000	1002	6.67 ± 0.20
200	15.57	7.8	6000	562	5.92 ± 0.24
300	16.54	7.6	65 536[b]	5887	6.21 ± 0.08
500	18.46	6.4	3000	315	5.96 ± 0.33
700	19.91	6.4	3000	298	6.18 ± 0.35
1000	21.40	6.0	3000	342	6.93 ± 0.36
1200	22.11	6.0	3000	334	7.18 ± 0.38
1500	22.89	6.0	3000	318	7.38 ± 0.40
2000	23.74	6.0	3000	301	7.78 ± 0.44
2500	24.32	6.0	3000	261	8.37 ± 0.51
3500	25.02	6.8	3000	253	10.54 ± 0.65

[a] $N_{r,s}$ are the trajectories leading to $SO + O$ formation with rate constant $k_s(T)$. [b] For $T = 300$ K, a large number of trajectories has been run to improve the accuracy of the product SO vibrational−rotational energy distribution.

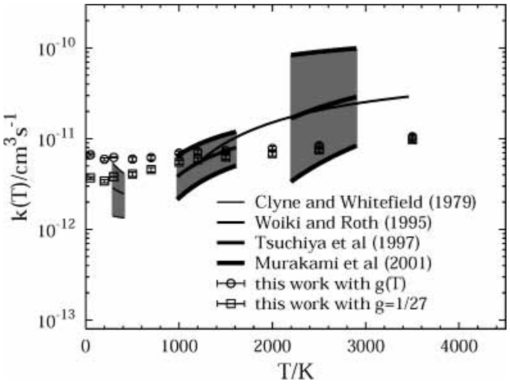

Figure 3. Calculated and experimental rate constants for the reaction $S + O_2 \rightarrow SO + O$.

reported rate constants were obtained using the appropriate temperature dependence for the electronic degeneracy factor $g(T)$ given in eq 2; the values calculated within the high-temperature-limit approximation using $g = 1/27$ can easily be obtained from the data reported in Table 4. The results for these two approximations are both displayed in Figure 3 over a wide range of temperatures together with available experimental data.[7−10] The error bars associated with the experimental results are also indicated by the shadowed areas which are delimited by the lines corresponding to the maximum errors when these are available. For the $S + O_2$ reaction, the calculated QCT results show a satisfactory agreement with the experimental data, being in most cases within the experimental error. Nevertheless, there appears to be some reactivity overestimation for low-temperature regimes, while an underestimation is observed at high temperatures. The overestimation at low temperatures can probably be attributed to small deficiencies in the potential energy surface, possibly an excessive attraction for near-C_{2v} paths referring to the $S - O_2$ approach. In fact, exploratory work using ad hoc modifications of the potential energy surface tending to diminish the attractiveness of the potential energy surface at the long-range regions has shown that the reactivity could be decreased to values close to the experimental ones at low temperatures. Unfortunately, such a tendency would also extend to the high-temperature regimes. Note that the underestimation of reactivity at high temperatures may be due to insufficient opening of the entrance channel or to exaggerated barriers near collinearity, although such a guess contradicts the existing ab initio results. It should also be noted that Murrell and co-workers[13,14] obtained thermal rate constant in good agreement with the experimental results at low temperatures but experienced difficulties in mimicking the correct dependence on temperature.[13] As already pointed out, their most recent surface[14] is also likely to suffer from wrong barrier localization. Finally, Lendvay et al[16] have also found an exaggerated reactivity which they have corrected with an ad hoc modification of the long-range part of the potential energy surface. Although we cannot discard that the present DMBE surface may suffer from small deficiencies (possibly, an excessive attraction at long-range regions), it is also true that there are well-known surface crossings that need to be taken into consideration before any serious attempt to achieve high accuracy can be done.

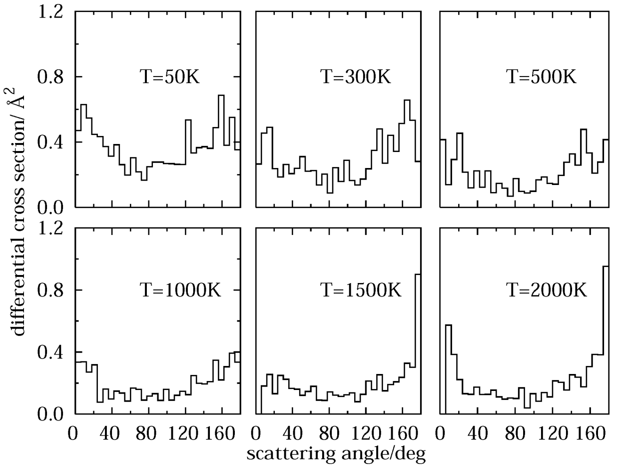

Figure 4. Differential cross-section for reaction $S + O_2 \rightarrow SO + O$ at several temperatures.

Despite not being experimentally available, we have calculated the differential cross sections for the reaction $S + O_2 \rightarrow SO + O$ at different temperatures, which are shown in Figure 4. The salient pattern is typical of a nondirect type reaction with formation of long-lived complexes. This can easily be inferred from the almost isotropic distribution of the differential cross sections as a function of the scattering angle. For $T = 300$ K, the formation of long-lived complexes can be corroborated from the analysis of the lifetime distributions of the complexes which are shown in Figure 5. This illustrates the distributions, percentages, and lifetimes of the three most relevant types of complexes which can be formed prior to dissociation through the available reactive channels. The most visible finding is the confirmation of the postulated[4] relevance of the SOO and OOS isomers in the reaction mechanism. In fact, almost all trajectories that dissociate to one of the reactive channels will evolve through the corresponding isomer, and there are a significant number of trajectories that even visit both isomers. Although the first observation can obviously be inferred from the potential energy surface topography (see Figure 1), the second offers new insights on the reaction behavior. Finally, we should note that about 25% of the trajectories visit the SO_2 isomer forming very long-lived complexes, with a mean average lifetime of about 1.5 ps.

The results for the reverse thermal reaction $O + SO \rightarrow S + O_2$ are given in Table 5 and Figure 6 using the appropriate temperature-dependent electronic degeneracy $g(T)$. Note that the effect of this temperature dependence does not appear relevant

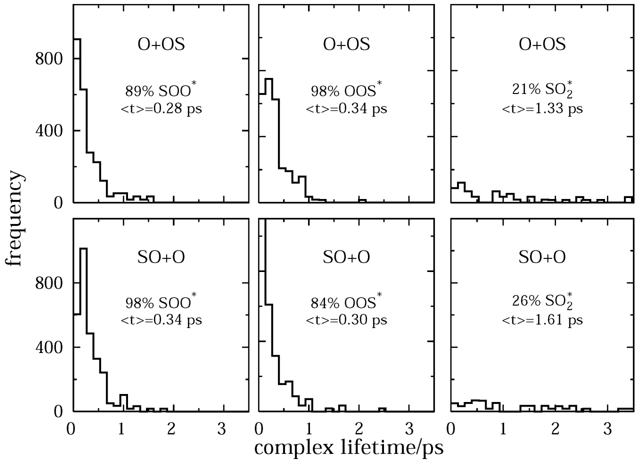

Figure 5. Complex-lifetime distributions for the reaction S + O_2 → O + OS/SO + O at $T = 300$ K. The various plots are best interpreted by looking at Figure 1. For example, starting from the bottom corner of the triangle to end at the top right-hand-side one, the results in the top line of panels show that 89% of the trajectories sample the SOO minimum on the left-hand-side (i.e., lead to SOO* complexes) while 98% visit the SOO right-hand-side minimum (OSS*). Of all trajectories, only 21% sample the deep SO_2 minimum ($SO_2^\star$). A corresponding interpretation holds for S + O formation.

TABLE 5: Trajectory Results for the O + SO Reaction[a]

T/K	$g(T)$	b_{max}/Å	N_t	$N_{r,s}$	$k_s(T)/10^{-12}$ cm^3 s^{-1}
500	22.27	7.4	3000	1	0.02 ± 0.02
700	23.38	6.8	6000	8	0.09 ± 0.03
1000	24.33	6.0	3000	10	0.21 ± 0.06
1200	24.73	6.0	3000	10	0.22 ± 0.07
1500	25.15	6.0	3000	14	0.34 ± 0.09
2000	25.58	6.8	3000	17	0.47 ± 0.11
2500	25.85	7.2	3000	34	1.04 ± 0.18

[a] $N_{r,s}$ are the trajectories leading to S + O_2 formation with rate constant $k_s(T)$.

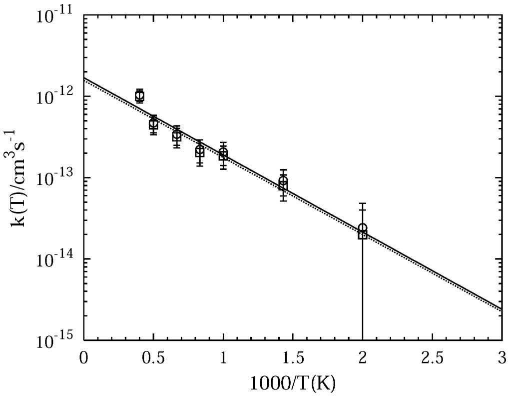

Figure 6. Calculated rate constants for the reaction O + SO → S + O_2. Symbols are as in Figure 3; the Arrhenius fits to the calculated values are indicated by the thin lines.

within the scale of Figure 6. Disregarding the usual statistical fluctuations, both results seem to follow an Arrhenius type form, as can be seen from the fitted curves (thin lines). There are no direct experimental results for this reaction, but the approximate experimental rate constants can be inferred from the equilibrium constant using the relation $K(T) = k_{-1}(T)/k_1(T)$. Instead of doing this, we have calculated the equilibrium constant directly from the QCT thermal rate coefficients for the forward and backward reactions. The calculated equilibrium constant for the process O + SO ⇌ O_2 + S is shown in Figure 7. The agreement with the analytical fit of Schofield[1] to the thermodynamic data of Gurvich et al[42] is good.

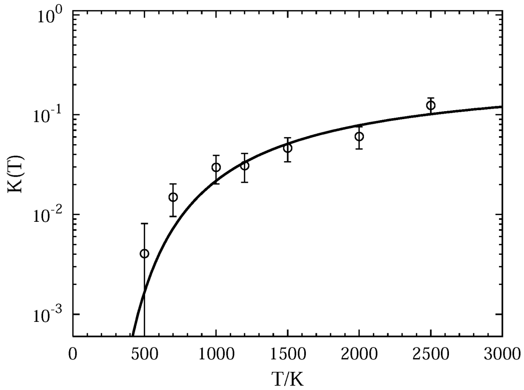

Figure 7. Calculated equilibrium constant for the process O + SO ⇌ S + O_2. The solid line is a fit to thermodynamic data.[1]

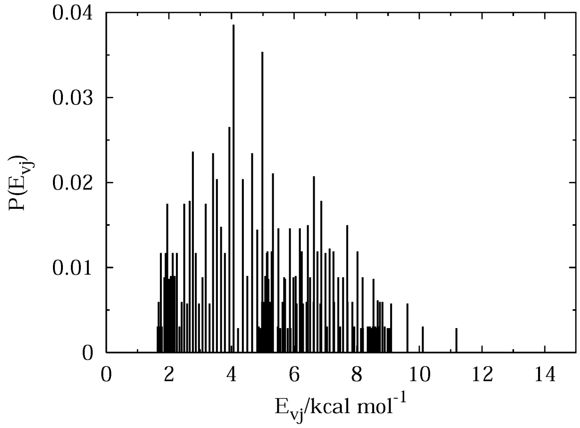

Figure 8. Product SO vibrational−rotational energy distribution obtained for S + O_2 collisions initially thermalized at $T = 300$ K.

4.1. Product Energy Distribution for the Reaction S + O_2 → SO + O. The quantum vibrational−rotational energy distribution of the product SO molecules in the thermalized S + O_2 collisions at $T = 300$ K is shown in Figure 8. For every trajectory, the assignment of the diatomic quantum levels has been made using the method of Muckerman,[43] where the energy is fitted to eq 5 in order to obtain the v and j quantum numbers. First, an approximation to the diatomic rotational quantum number j' is obtained from

$$j'(j' + 1) = L^2/\hbar^2 \tag{9}$$

where L is the diatomic classical angular momentum. Then, starting with a rigid-rotor approximation for the rotational energy $E'_{rot} = B_e j'(j' + 1)$, successive iterative approximations to the vibrational quantum number v', vibrational energy E_{vib}, and rotational energy E_{rot} are carried out from the total diatomic internal energy E_{int} as follows:

$$E'_{vib} = E_{int} - E'_{rot} \tag{10}$$

$$v' + \frac{1}{2} = \frac{1}{2}\omega_e/\omega_e x_e - \frac{1}{2}[(\omega_e/\omega_e x_e)^2 - 4E'_{vib}/\omega_e x_e]^{1/2} \tag{11}$$

$$B'_v = B_e - \left(v' + \frac{1}{2}\right)\alpha_e \tag{12}$$

$$E_{rot} = B'_v j'(j' + 1) - D_e[j'(j' + 1)]^2 \tag{13}$$

$$E_{vib} = E_{int} - E_{rot} \tag{14}$$

The procedure finishes when the vibrational and rotational energies are converged within 0.001 cm^{-1} and 0.1 cm^{-1},

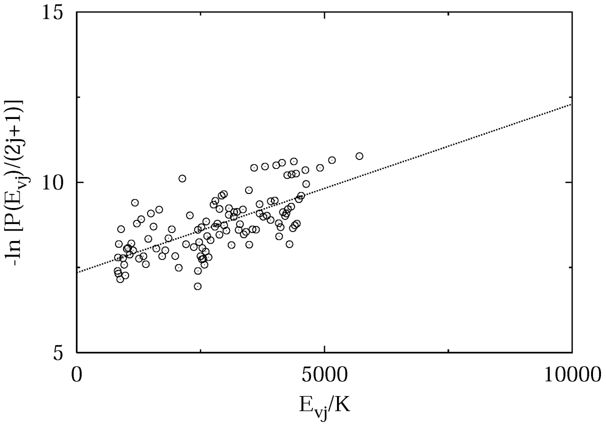

Figure 9. Plot of $\ln[P(E_{vr})/(2j+1)]$ vs E_{vr} for the product diatomic SO obtained in S + O_2 collisions initially thermalized at $T = 300$ *K*.

respectively. Finally, j' and v' are assigned to integer values by the usual binning procedure. Figure 9 shows the logarithm of the probability for each vibrational−rotational energy divided by its degeneracy $\ln[P(E_{vr}/(2j+1)]$ as a function of E_{vr}. Note that for a perfectly thermalized distribution, the results should follow the straight line $\ln[P(E_{vr}/(2j+1)] = \ln Q_{vr}(T) - E_{vr}/T$. The actual fit leads to $7.35 \pm 0.16 + E_{vj}/2019 \pm 210$. Although a linear plot is possible on an average sense, this may simply reflect either a certain memory of the initial thermalized distribution or the fact that the dynamics involves substantially long-lived complexes.[44] Thus, it is unclear to what extent the results imply a Boltzmann distribution on the products. In fact, an attempt has been made to clarify this point by drawing similar plots for specific final vibrational states. Although not shown, the results were once more not conclusive with respect to the products thermalization.

5. Conclusions

Dynamics studies of the reaction S + $O_2 \rightarrow$ SO + O and its reverse have been performed using an accurate single-valued double many-body expansion (DMBE) potential energy surface for the ground electronic state of the sulfur dioxide. The calculated thermal rate constants are found to be in fair agreement with the available experimental data. Although one can attribute part of the disagreement to remaining inaccuracies in the potential energy surface, any improvement of the latter is probably justified only when accurate nonadiabatic dynamics calculations are carried out (of course, this implies a multi-sheeted potential energy surface[25]) and the experimental error bars are reduced.

Acknowledgment. This work has the support of Fundação Para a Ciência e Tecnologia, Portugal, under Program PRAXIS XXI.

References and Notes

(1) Schofield, K. *Combust. Flame* **2001**, *124*, 137.

(2) Homman, K. H.; Krome, G.; Wagner, H. G. *Ber. Bunsen-Ges. Phys. Chem.* **1968**, *72*, 998.

(3) Fair, R. W.; Thrush, B. A. *Trans. Faraday Soc.* **1969**, *65*, 1557.

(4) Fair, R. W.; Van Roodselaar, A.; Strausz, O. P. *Can. J. Chem.* **1971**, *49*, 1659.

(5) Davies, D. D.; Klemm, R. B.; Pilling, M. *Int. J. Chem. Kinet.* **1972**, *4*, 367.

(6) Donovan, R. J.; Little, D. J. *Chem. Phys. Lett.* **1972**, *13*, 488.

(7) Clyne, M. A. A.; Whitefield, P. D. *J. Chem. Soc., Faraday Trans. 2* **1979**, *75*, 1327.

(8) Woiki, D.; Roth, P. *Int. J. Chem. Kinet.* **1995**, *27*, 59.

(9) Tsuchiya, K.; Kamiya, K.; Matsui, H. *Int. J. Chem. Kinet.* **1997**, *29*, 57.

(10) Murakami, Y.; Kosugi, M.; Susa, K.; Kabayashi, T.; Fugii, N. *Bull. Chem. Soc. Jpn.* **2001**, *74*, 1233.

(11) Schofield, K. *J. Phys. Chem. Ref. Data* **1973**, *2*, 25.

(12) Atkinson, R.; Baulch, D. L.; Cox, R. A.; Hampson, R. F.; Kerr, J. A.; Rossi, M. J.; Troe, J. *J. Phys. Chem. Ref. Data* **1997**, *26*, 1329.

(13) Murrell, J. N.; Craven, W.; Farantos, S. C. *Mol. Phys.* **1983**, *49*, 1077.

(14) Craven, W.; Murrell, J. N. *Mol. Phys.* **1987**, *83*, 1733.

(15) Murrell, J. N.; Craven, W.; Vincent, M.; Zhu, Z. H. *Mol. Phys.* **1985**, *56*, 839.

(16) Lendvay, G.; Schatz, G. C.; Harding, L. B. *Faraday Discuss.* **1995**, *102*, 389.

(17) Bastida, A.; Zúñiga, J.; Requena, A. *J. Mol. Spectrosc.* **1989**, *136*, 185.

(18) Kauppi, E.; Halonen, L. *J. Chem. Phys.* **1992**, *96*, 2933.

(19) Zúñiga, J.; Bastida, A.; Requena, A. *J. Chem. Phys.* **2001**, *115*, 139.

(20) Weis, B. Ph.D. Thesis, University of Frankfurt, Germany, 1991.

(21) Varandas, A. J. C.; Rodrigues, S. J. P. *Spectrochim. Acta, Part A* **2002**, *58*, 629.

(22) Rodrigues, S. P. J.; Sabín, J. A.; Varandas, A. J. C. *J. Phys. Chem. A* **2002**, *106*, 556.

(23) Varandas, A. J. C. *Adv. Chem. Phys.* **1988**, *74*, 255.

(24) Varandas, A. J. C. In *Lecture Notes in Chemistry*; Laganá, A., Riganelli, A., Eds.; Springer: Berlin, 2000; Vol. 75, p 33.

(25) Varandas, A. J. C. Modeling and interpolation of global multi-sheeted potential energy surfaces. In *Conical Intersections: Electronic Structure, Dynamics and Spectroscopy*; Yarkony, D., Köppel, H., Domcke, W., Eds.; World Scientific Publishing: Singapore, in press.

(26) Varandas, A. J. C. *Chem. Phys. Lett.* **1987**, *138*, 455.

(27) Bunker, D. L. *Methods Comput. Phys.* **1971**, *10*, 287.

(28) Porter, R. N.; Raff, L. M. In *Modern Theoretical Chemistry, Dynamics of Molecular Collisions*; Miller, W., Ed.; Plenum: New York, 1976; Vol. II, part B, p 1.

(29) Peslherbe, G. H.; Wang, H.; Hase, W. L. *Adv. Chem. Phys.* **1999**, *105*, 171.

(30) Varandas, A. J. C.; Pais, A. A. C. C.; Marques, J. M. C.; Wang, W. *Chem. Phys. Lett.* **1996**, *249*, 264.

(31) Marques, J. M. C.; Wang, W.; Pais, A. A. C. C.; Varandas, A. J. C. *J. Phys. Chem.* **1996**, *100*, 17513.

(32) Hase, W. L. MERCURY: a general Monte Carlo classical trajectory computer program, QCPE#453. An updated version of this code is VENUS96: Hase, W. L.; Duchovic, R. J.; Hu, X.; Komornik, A.; Lim, K. F.; Lu, D.-H.; Peslherbe, G. H.; Swamy, K. N.; van de Linde, S. R.; Varandas, A. J. C.; Wang, H.; Wolf, R. J. *QCPE Bull.* **1996**, *16*, 43.

(33) Truhlar, D. G. *J. Chem. Phys.* **1972**, *56*, 3189.

(34) Muckerman, J. T.; Newton, M. D. *J. Chem. Phys.* **1972**, *56*, 3191.

(35) NIST atomic spectra database, http://physics.nist.gov/cgi-bin/atdata/mainasd.

(36) Martin, W. C.; Zalubas, R.; Musgrove, A. *J. Phys. Chem. Ref. Data* **1990**, *19*, 821.

(37) Varandas, A. J. C.; Pais, A. A. C. C. In *Theoretical and Computational Models for Organic Chemistry*; Formosinho, S., Czismadia, I., Arnaut, L., Eds.; Kluwer: Dordrecht, The Netherlands, 1991; p 55.

(38) Varandas, A. J. C.; Brandão, J.; Pastrana, M. R. *J. Chem. Phys.* **1992**, *96*, 5137.

(39) Herzberg, G. *Molecular Spectra and Molecular Structure. I. Spectra of Diatomic Molecules*; van Nostrand: New York, 1950.

(40) Porter, R. N.; Raff, L. M.; Miller, W. H. *J. Chem. Phys.* **1975**, *63*, 2214.

(41) Rodrigues, S. P. J.; Varandas, A. J. C. *J. Phys. Chem.* **1998**, *102*, 6266.

(42) Gurvich, L. V., Veyts, I. V., Alcock, C. B., Eds.; *Thermodynamic Properties of Individual Substances*, 4th ed.; Hemisphere: New York, 1989; Volume 1, Part 2: Tables.

(43) Muckerman, J. T. *J. Chem. Phys.* **1971**, *54*, 1155.

(44) Varandas, A. J. C.; Llanio-Trujillo, J. L. *J. Theor. Comput. Chem.* **2002**, *1*, 31.